Mechanoadaptive morphing gel electrolyte enables flexible and fast-charging Zn-ion batteries with outstanding dendrite suppression performance

Faqing Cao[1], Baohu Wu[2], Tianyu Li[3], Shengtong Sun[1] (✉), Yucong Jiao[1] (✉), and Peiyi Wu[1] (✉)

[1] *State Key Laboratory for Modification of Chemical Fibers and Polymer Materials, College of Chemistry Chemical Engineering and Biotechnology & Center for Advanced Low-dimension Materials, Donghua University, Shanghai 201620, China*

[2] *Jülich Centre for Neutron Science (JCNS) at Heinz Maier-Leibnitz Zentrum (MLZ) Forschungszentrum Jülich, Lichtenbergstr. 1, 85748 Garching, Germany*

[3] *Division of Energy Storage, Dalian National Laboratory for Clean Energy, Dalian Institute of Chemical Physics, Chinese Academy of Sciences, Dalian 116023, China*

ABSTRACT

The safe, flexible, and environment-friendly Zn-ion batteries have aroused great interests nowadays. Nevertheless, flagrant Zn dendrite uncontrollably grows in liquid electrolytes due to insufficient surface protection, which severely impedes the future applications of Zn-ion batteries especially at high current densities. Gel electrolytes are emerging to tackle this issue, yet the required high modulus for inhibiting dendrite growth as well as concurrent poor interfacial contact with roughened Zn electrodes are not easily reconcilable to regulate the fragile Zn/Zn^{2+} interface. Here we demonstrate, such a conflict may be defeated by using a mechanoadaptive cellulose nanofibril-based morphing gel electrolyte (MorphGE), which synergizes bulk compliance for optimizing interfacial contact as well as high modulus for suppressing dendrite formation. Moreover, by anchoring desolvated Zn^{2+} on cellulose nanofibrils, the side reactions which induce dendrite formation are also significantly reduced. As a result, the MorphGE-based symmetrical Zn-ion battery demonstrated outstanding stability for more than 100 h at the high current density of 10 mA·cm^{-2} and areal capacity of 10 mA·h·cm^{-2}, and the corresponding Zn-ion battery delivered a prominent specific capacity of 100 mA·h·g^{-1} for more than 500 cycles at 20 C. The present example of engineering the mechanoadaptivity of gel electrolytes will shed light on a new pathway for designing highly safe and flexible energy storage devices.

KEYWORDS

Zn-ion batteries, dendrite growth, interfacial adaptivity, gel electrolytes, fast-charging

1 Introduction

With the rapid development of modern society, flexible and wearable battery devices with high safety and eco-friendliness are worldwide needed nowadays [1, 2]. Zn-ion batteries, with aqueous electrolyte and Zn metal as anode, have been emerged as one of the most potential candidates for the earth abundance of Zn, intrinsically safe aqueous electrolyte, and relatively low cost. Meanwhile, the Zn metal anode owns a high theoretical capacity of around 820 mA·h·g^{-1}, low redox potential (−0.76 V vs. the standard hydrogen electrode), and a volumetric capacity of around 3 times higher than lithium, benefitting from the two-electron redox of Zn [3]. Nevertheless, the notorious dendrite issue that would rupture to death Zn metal and/or lead to severe safety problem by causing short circuit, remains to be urgently settled before Zn-ion batteries enter practical applications [4–7]. Noteworthily, the main reason for dendrite formation is that Zn anode surface is not atomic-level smooth, which will provide different nucleation barriers and cause the uneven nucleation and uncontrollable growth of Zn metal in liquid electrolytes (Fig. 1(a)). With further deposition after nucleation, Zn crystals with irregular shapes begin to form on the metal surface resulting in a roughened surface in large scale, which further exacerbates dendrite growth. In addition, side reaction induced by Zn^{2+} solvation structure ($[Zn(H_2O)_6]^{2+}$) is another critical factor that shows significant impact on Zn metal nucleation and formation. The activated water molecules in $[Zn(H_2O)_6]^{2+}$ are inclined to corrode Zn metal even in neutral electrolytes. In particular, at high current densities, the low overpotential will aggravate side reactions such as hydrogen evolution reaction (HER), which will cause electrode resistance increase, lower the inferior Zn/Zn^{2+} reversibility during charge–discharge, and finally lead to dendrite formation [8–11].

To tackle the above issues, a lot of endeavors have been conducted such as designing specific structures for both Zn anodes and inorganic cathodes [4, 12–21], adjusting electrolyte compositions [5, 22–26], introducing artificial layers [9], or employing solid or quasi-solid gel polymer electrolytes [7, 8, 27–33]. Among them, gel electrolytes are proved to be very attractive for its flexibility, structural designability, high ionic conductivity, and importantly, mechanical integrity to suppress

Address correspondence to Shengtong Sun, shengtongsun@dhu.edu.cn; Yucong Jiao, yucong.jiao@dhu.edu.cn; Peiyi Wu, wupeiyi@dhu.edu.cn

dendrite growth. In general, a gel electrolyte with low modulus may still be easily and irreversibly broken by Zn metal volume changes, leading to a deteriorated dendrite-suppressing ability. A spontaneous solution is to increase the modulus of gel electrolyte to help inhibit dendrite formation at the Zn metal/electrolyte interface, e.g., by involving multiple crosslinks or nanofillers [34–36]. Nonetheless, simply increasing the moduli of gel electrolytes often means a higher rigid elasticity; when the interface is not smooth in the case of flexible electrodes or the above-mentioned gradual roughening during cycling, these high-modulus gel electrolytes would concurrently incur severe interfacial contact issues (Fig. 1(b)) [37]. Consequently, side reactions between Zn anode and free liquid electrolyte still occur in the voids resulting in small dendrites, which severely influence battery performance. To improve the interfacial contact with roughened Zn anodes, the bulk compliance of gel electrolytes that can adapt to rough surfaces is highly required [38–40]. However, in terms of mechanical concerns, the conflict between high modulus for inhibiting dendrite formation and bulk compliance for good interfacial contact is not easily reconcilable for conventional rigid-elastic gel electrolytes. Indeed, nearly all the current gel-electrolyte-based Zn-ion batteries delivered unsatisfying dendrite and side reaction suppression performance at high current densities [41], which may mainly arise from the insufficient interfacial adaptability of gel electrolytes over roughened Zn anodes [41].

To challenge this paradigm, here we report a mechanoadaptive cellulose nanofibril-based morphing gel electrolyte (MorphGE) with both high modulus and bulk plasticity that meet both the interfacial and mechanical requirements facing current gel electrolytes (Fig. 1(c)). Comparing with conventional gel electrolytes based on a simple polymer chain network, the present MorphGE possesses the following advantages: 1) Mechanically, the as-engineered MorphGE exhibits high plasticity with a very short linear viscoelastic (LVE) region of 2%. In the case of gel deformations caused by the assembly process or the gradually roughened electrode surface during cycling, the plasticity can significantly improve interfacial contact and effectively optimize surface protection to harmonize Zn metal nucleation. 2) The MorphGE is hierarchically assembled from massive cellulose nanofibrils resulting in a unique layer-like structure and very high modulus of ~ 1.48 MPa, which not only helps suppress dendrite formation but also guide the homoepitaxial uniform deposition of Zn metal to grow horizontally with a hexagonal structure. 3) The cellulosic nature of MorphGE with abundant hydroxyl groups for coordinating Zn ions, could regulate its solvation structure of $[Zn(H_2O)_6]^{2+}$ to $[Zn(H_2O)_x]^{2+}$ ($x < 6$), hence reducing the desolvation energy of solvation structures to both facilitate Zn-ion reversibility and suppress side reactions. Owing to the above merits by synergizing bulk compliance, high modulus, and Zn-ion solvation structure regulation, the present MorphGE can not only astonishingly inhibit dendrite growth even at high current densities and areal capacities, but also exhibit outstanding rate performance and cycling stability, which are superior to most of currently reported Zn-ion batteries using gel electrolytes and liquid electrolytes.

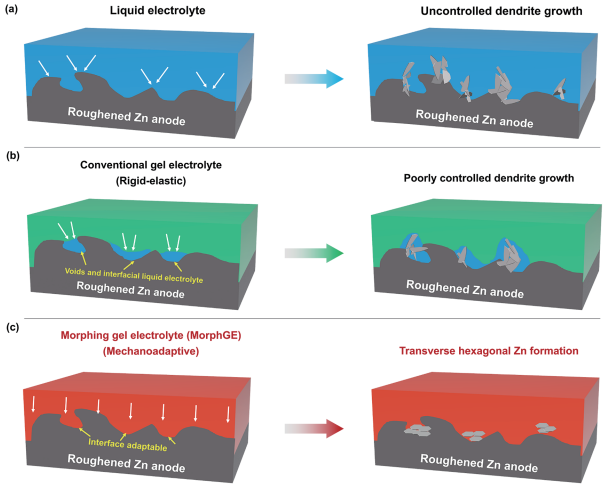

Figure 1 Schematic growth of Zn dendrites in the cases of three different types of electrolytes. (a) liquid electrolyte, (b) conventional rigid-elastic gel electrolyte, and (c) high-modulus, mechanoadaptive MorphGE. The liquid electrolyte has excellent contact with rough electrode, yet no inhibiting ability for dendrite growth. Conventional rigid-elastic gel electrolyte has poor mechanical adaptability and thus many voids will be generated in contact with rough electrode, causing uneven growth of dendrites. In sharp contrast, MorphGE adapts to the surface of electrode resulting in an interlocked structure, which can largely reduce interfacial contact resistance and promote uniform nucleation.

2 Experimental

2.1 Materials

Lithium chloride (LiCl), ethanol, N,N-dimethylacetamide (DMAc), and commercial filter paper were obtained from Shanghai Titan Scientific Co., Ltd. Acrylamide, 2,2'-azobis(2-methylpropionamidine) dihydrochloride (V50), N,N'-methylenebisacrylamide (BIS), $Mn(CH_3COO)_2{\cdot}4H_2O$, 1-methyl-2-pyrrolidinone (NMP), $MnSO_4$ and $KMnO_4$ were purchased from Sigma-Aldrich Co., Ltd. W0S1009 carbon cloth was purchased from Ce-Tech Co., Ltd. TGP-H-060 carbon paper was purchased from TORAY Co., Ltd. Carboxylated carbon nanotubes (CNT) were obtained from Suzhou Tanfeng Tech Co., Ltd. $ZnSO_4{\cdot}7H_2O$ and zinc plates were purchased from Sinopharm Chemical Reagent Co., Ltd. Zinc foil was obtained from Qingyuan Metal Co., Ltd.

2.2 Preparation of MorphGE

The regenerated cellulose-based MorphGE was prepared with reference to the previous literature with a slight modification [42]. Briefly, commercial filter paper was washed three times with water, ethanol and DMAc in sequence, and then dried at 60 °C. LiCl and DMAc were vigorously stirred to achieve a LiCl/DMAc solution with a concentration of 8%. Afterwards, 1.5 g of as-treated commercial filter paper was added to 98.5 g of the above-mentioned LiCl/DMAc solution and dissolved for 24 h to form a 1.5 wt.% cellulose solution. Finally, the insoluble portion was removed by centrifugation at 10,000 rpm for 3 times, and the supernatant cellulose solution was retained. The obtained cellulose solution was scraped into a rectangular frame with a thickness of 0.5 mm on a glass plate. Exposing the solution in the air (humidity ~ 40%) for 24 h induced gelation of cellulose nanofibrils through the formation of hydrogen bonds. The obtained cellulose organogel was then solvent exchanged with ethanol and deionized water in turn, cut into discs with a diameter of 19 mm, and immersed in a 2 M $ZnSO_4$/0.1 M $MnSO_4$ aqueous solution for later use.

2.3 Preparation of polyacrylamide (PAAm) gel electrolyte

1.5 g of acrylamide monomer was added to 8.5 g of a mixed solution of 2 M $ZnSO_4$ and 0.1 M $MnSO_4$, and stirred at room temperature until completely dissolved. Then, 1.5 mg of the initiator V50 and 1.5 mg of the crosslinker BIS were added to the above solution, and stirred at room temperature for 1 h. The

solution was photo-initiated in the mold for 20 min to obtain the cross-linked, highly elastic PAAm gel electrolyte.

2.4 Preparation of MnO_2/CNT cathode

The MnO_2/CNT composite was prepared via a typical hydrothermal method. 0.15 g of carboxylated CNT was dispersed into 150 mL of water uniformly, before 2.94 g of $Mn(CH_3COO)_2{\cdot}4H_2O$ was added to the mixture. Afterwards, 1.27 g of $KMnO_4$ was slowly dropped into the solution, and sonicated for 30 min before being transferred into a Teflon-lined autoclave and heated at 120 °C for 12 h. The resulting mixture was finally centrifuged and washed three times with water to obtain the MnO_2/CNT composite. For cathode preparation, the NMP solution of CNT/MnO_2, acetylene black, and poly(vinylidene fluoride) (PVDF) were mixed uniformly at a ratio of 7:2:1, and then coated on the carbon paper, before drying in a vacuum oven at 60 °C for 12 h.

2.5 Preparation of Zn anode

The zinc anode for semi-cell was cut directly from pure zinc foil with a thickness of 0.3 mm and a length and a width of 1 cm × 1 cm. The zinc anode used in the flexible battery was prepared by electroplating zinc metal onto a carbon cloth with CHI 760D electrochemical workstation, where zinc metal plate was used as reference and counter electrode, carbon cloth as working electrode, and the electroplating was carried out for 30 min at the current density of 15 mA·cm^{-2}.

2.6 Characterizations

Nicolet iS50 spectrometer with attenuated total reflection (ATR) and X-ray photoelectron spectrometer (XPS, Escalab 250Xi) were employed to study the interactions between cellulose and zinc ions. Powder X-ray diffractometer (XRD, Rigaku D/max-2550VB+/PC) was used to verify the crystalline states of MnO_2/CNT composite and zinc foil. The morphologies were observed by a LaB_6 scanning electron microscope (SEM, JSM-IT300) and a transmission electron microscope (TEM, JEM-2100). Thermo Scientific HAAKE MARS modular advanced rheometer was used to explore the rheological behavior of cellulose and PAAm gels. The mechanical test was carried out on the universal testing machine (UTM2103, Shenzhen Sunstechnology Co., Ltd.). The polarized images of MorphGE (without salts) were taken on an Olympus BX53-P Polarizing Microscope. Raman spectroscopy for the electrolyte, MorphGE and PAAm gel electrolyte was conducted on Thermo Fisher Scientific DXR2xi.

2.7 Electrochemical measurement

The CR2032-type coin cells were assembled for electrochemical performance assessment. The galvanostatic charge/discharge tests were performed on a Neware battery Tester. The CHI 760D was employed for cyclic voltammetry (CV) test at different scanning rates between the voltages of 0.8–1.85 V, and for electrochemical impedance spectroscopy (EIS) characterization at a frequency of 100 kHz–0.1 Hz. The transference number of zinc ions was calculated by testing the EIS at 10 kHz–0.1 Hz before and after the symmetrical Zn cell was polarized under 20 mV for 1,000 s. The calculating equation is as follows

$$t_{Zn^{2+}} = \frac{I_S(\Delta V - I_0 R_0)}{I_0(\Delta V - I_S R_S)} \quad (1)$$

where I_0 is initial current; I_s is steady-state current; R_0 is initial resistance; R_s is steady-state resistance after polarization; ΔV is polarization voltage.

The ionic conductivity was measured by EIS from 10 kHz to 0.1 Hz, and calculated as follows

$$\sigma = \frac{l}{R_b \times S} \quad (2)$$

where l is polymer electrolyte/separator thickness; R_b is bulk resistance; S is area of the polymer electrolyte/separator.

2.8 Small-angle X-ray scattering (SAXS)

SAXS experiments were performed at the Shanghai Synchrotron Radiation Facility (SSRF) beamline BL16B (Shanghai, China) at an X-ray energy of 10.0 keV which corresponds to a wavelength of λ = 1.24 Å. Samples were measured perpendicular to the beam with the sample–detector distances of 1.83 m to cover the scattering vector $\boldsymbol{q}$ range from 0.1 to 5.3 nm^{-1} ($\boldsymbol{q}$ is the scattering vector, $\boldsymbol{q} = (4\pi/\lambda)\sin(\theta)$, and 2θ is the scattering angle). The scattering patterns were obtained with a short exposure time (120 s). Air as background was subtracted. The SAXS patterns were azimuthally and radially averaged to obtain the intensity profiles. The rod radius was obtained by fitting with a flexible cylinder model [43].

2.9 Density functional theory (DFT) calculations

DFT calculations were performed with Gaussian 16 package. The PBE0 (PBE: Perdew–Burke–Ernzerhof) hybrid functional at def2-SVP level of basis set including the atom-pairwise dispersion (DFT-D3) correction with Becke–Johnson (BJ) damping, was applied for geometry optimization. The implicit universal water solvation model based on solute electron density (SMD) was applied in all calculations. Single point calculations of the optimized structures were carried out at PBE0/def2-QZVP3 also including the DFT-D3(BJ) correction.

3 Results and discussion

3.1 Structure and plasticity of MorphGE

The mechanoadaptive MorphGE was derived from processing readily available filter papers via LiCl/DMAc dissolution and hydrogen bond-induced gelation, followed by being soaked in the liquid electrolyte ($ZnSO_4$/$MnSO_4$, 2 M/0.1 M) for 12 h. As shown in Fig. 2(a), the as-prepared MorphGE is fully transparent and homogenous. Interestingly, a unique layer-like structure of MorphGE was observed from SEM and TEM images (Fig. 2(b) and Fig. S1 in the Electronic Supplementary Material (ESM)). Polarized light microscopic observations reveal no in-plane orientations yet the unidirectional orientation of the layers parallel to the top surface of the film (Figs. S2 and S3 in the ESM). It is presumed that the cellulose layers of MorphGE are unidirectionally aligned but its constituent units are randomly oriented. This structural model is further supported by SAXS results with the inset two-dimensional (2D) image showing no structurally preferential orientation (Fig. 2(c)). At high $\boldsymbol{q}$, the power law exponent is around −1, which indicates a rod-like scattering. The low $\boldsymbol{q}$ scattering curve shows scattering between $\boldsymbol{q}^{-2}$ and $\boldsymbol{q}^{-3}$ indicating a mass fractal organization. The rod radius of the interwoven constituent cellulose nanofibrils was determined to be ~ 2 nm by fitting with a flexible cylinder model. Moreover, the average mesh size between nanofibrils was roughly estimated to be ca. 3 nm based on the turning point of the scattering curve at the $\boldsymbol{q}$ value of about 2 nm^{-1} ($d = 2\pi/\boldsymbol{q}$).

The MorphGE film possesses excellent flexibility and mechanical strength even when the thickness is only 100 μm. The tensile stress–strain curve indicates the maximum elongation of 128%, tensile strength of 3.22 MPa, and Young's modulus of 1.48 MPa (Fig. S4 in the ESM), higher than most of currently

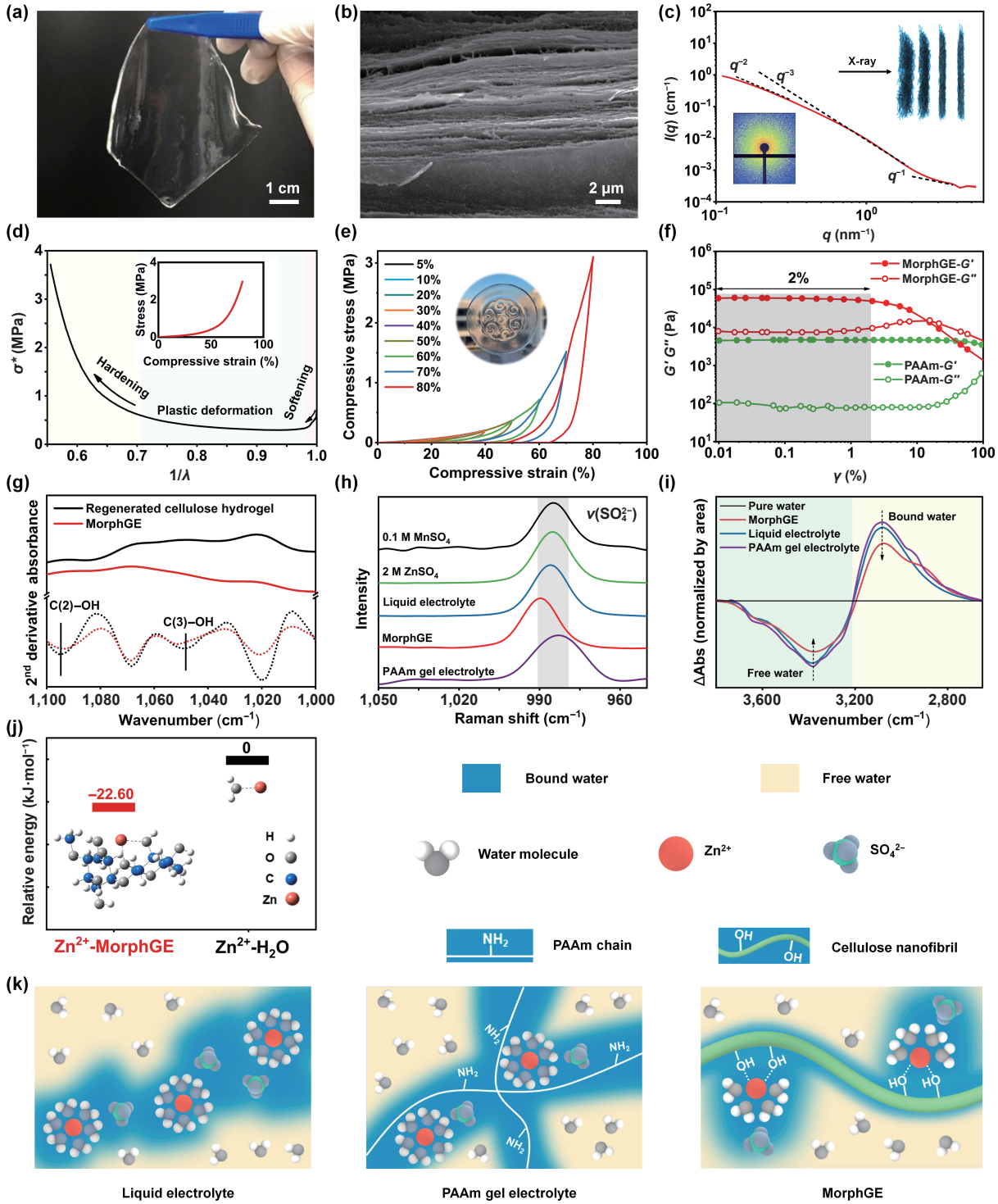

Figure 2 (a) Optical image of MorphGE. (b) Cross-sectional SEM image of freeze-dried MorphGE (without salt). (c) SAXS scattering profile of MorphGE (without salt; the insets are corresponding 2D image and schematic hierarchical structure). (d) Mooney–Rivlin plot of MorphGE derived from the compressive stress–strain curve (inset). Deformation ratio, $\lambda = \varepsilon + 1$; Mooney stress, $\sigma^* = \sigma/(\lambda - \lambda^{-2})$. (e) Cycling compressive stress–strain curves with increasing strain amplitudes. (f) Amplitude sweep rheological data of MorphGE and PAAm gel electrolyte. The two hydrogels have an equal solid content of 15 wt. % (excluding salts). (g) ATR-Fourier transform infrared spectroscopy (FTIR) and corresponding second-derivative spectra of regenerated cellulose hydrogel and MorphGE. (h) Raman spectra of liquid electrolyte, MorphGE, and PAAm gel electrolyte. (i) Differential ATR-FTIR spectra of liquid electrolyte, MorphGE, and PAAm gel electrolyte. The IR spectrum of pure water was used as reference, and all the spectra were normalized by the integral area. (j) DFT calculations for the relative binding energies of Zn^{2+} with different species. (k) Schematic diagrams of the solvation structures of Zn ions in liquid electrolyte, PAAm gel electrolyte, and MorphGE, respectively.

reported hydrogel electrolytes for Zn-ion batteries [31, 36]. The swelling ratio and corresponding mechanical strength were also examined after soaking for 72 h in electrolyte. As shown in Fig. S5 in the ESM, no obvious swelling was observed in the MorphGE after soaking. The tensile stress–strain curve of MorphGE after soaking exhibits a slightly higher tensile strength and lower elongation than regenerated cellulose gel, which may be due to the role of Zn^{2+} in crosslinking cellulose hydroxyl groups (Fig. S4 in the ESM). Compression test that resembles the assembly process of batteries is presented in the Mooney–Rivlin plot to show the apparent changes of gel's modulus with compressive strain (Fig. 2(d)). Three stages can be identified, i.e., force-induced softening ($1/\lambda \approx 1$–0.98, corresponding to $\varepsilon \approx 0$–0.02), plastic deformation ($1/\lambda \approx 0.98$–0.71, corresponding to $\varepsilon \approx 0.02$–0.41),

and final hardening ($1/\lambda \approx 0.71–0.56$, corresponding to $\varepsilon \approx 0.41–0.80$). A long plastic deformation stage ranging from 2% to 41% strongly supports that MorphGE is shape-morphable. The shape-morphing feature is believed to arise from the irreversible slipping of cellulose nanofibrils upon deformation which then gain a new thermodynamically stable state via the reformation of dynamic hydrogen bonds among cellulose chains. The plasticity of MorphGE is further confirmed by the gradient compression cycle test (Fig. 2(e)), indicating that MorphGE cannot recover to the original thickness upon compression. As a demonstration, specific patterns may be printed onto the gel by pressing a mold on it and holding for a certain period (see the inset image in Fig. 2(e)). Furthermore, the shape morphing feature of MorphGE is also evidenced by a very short LVE region of about 2% (Fig. 2(f)). For comparison, the commonly used highly elastic PAAm hydrogel electrolyte exhibits a long LVE region of about 20%, yet much lower storage and loss moduli than MorphGE. Note that, for coin-cell tests, the gel electrolyte is generally compressed by ~ 20% in the assembly process. As tested, pre-compression by 20% would further increase MorphGE's moduli by almost one order of magnitude, yet no significant effect on the LVE region was observed (Fig. S6 in the ESM). It is noted that, owing to the unique hierarchical structure assembled from cellulose nanofibrils, the synergized plasticity and high modulus of MorphGE are distinct from all the currently reported gel electrolytes for Zn-ion batteries, which would contribute to both gel-electrode interfacial adaptability and dendrite suppression during plating, critical for the safety and stability of Zn-ion batteries especially at high current densities.

3.2 Internal interactions in MorphGE

Besides interfacial adaptability, the proper interactions between Zn ions and MorphGE are also important to get rid of side reactions. As reflected by infrared (IR) spectral comparison (Fig. 2(g)), soaking regenerated cellulose hydrogel in $ZnSO_4/MnSO_4$ electrolyte causes the wavenumber shift of the C(3)–OH stretching peak at 1,048 to 1,051 cm^{-1}, and C(2)–OH stretching at 1,096 cm^{-1} shifts to 1,093 cm^{-1}, suggesting the strong interactions between Zn^{2+} and cellulose nanofibrils. As previously reported, Zn^{2+} in the form of hydrates would compete with the protons of cellulose hydroxyl groups (Fig. S7 in the ESM), and thus weaken its intrinsic hydrogen bonding networks [44–46]. Similar shifts were also observed in the Zn $2p_{3/2}$ and O 1s XPS spectra (Fig. S8 in the ESM). To further elucidate the effect of cellulose–Zn^{2+} interactions on the whole gel electrolyte, we employed Raman and differential IR spectroscopy to examine the status of sulfate ions and water clustering. Interestingly, as illustrated in Fig. 2(h), compared with liquid electrolyte, the $\nu(SO_4^{2-})$ band in MorphGE shifts to a higher frequency, while mainly peak broadening takes place for conventional PAAm gel electrolyte [5, 11]. This result reveals that the ion complexation between Zn^{2+} and sulfate is disrupted by cellulose nanofibrils in MorphGE, leading to a less coordinated state of sulfate ions. In comparison, in PAAm gel electrolyte, the ion complexation between Zn^{2+} and sulfate is not significantly influenced, yet the surrounding water environment of sulfate is more diversified in the presence of PAAm chain networks, resulting in apparent Raman peak broadening.

The Zn^{2+}-cellulose chelation also influences the relative content of bound water and free water. As shown in the differential IR spectra (Fig. 2(i)), more free water at the expense of bound water is observed in MorphGE than those in liquid electrolyte and PAAm gel electrolyte. It is thus presumed that the stable hexahydrate form of Zn^{2+} ($[Zn(H_2O)_6]^{2+}$) may predominate in liquid electrolyte and PAAm gel electrolyte, while cellulose hydroxyl groups anchor plenty of desolvated Zn^{2+} via hydrogen bonding, along with the release of more water molecules from $[Zn(H_2O)_6]^{2+}$. In other words, the observed amount increase of free water in the case of MorphGE should be the direct consequence of desolvated $[Zn(H_2O)_6]^{2+}$ as reflected by the Raman peak shift of $\nu(SO_4^{2-})$. To further demonstrate this conclusion, the binding energies of Zn^{2+} to MorphGE and H_2O were calculated by DFT, respectively. As exhibited in Fig. 2(j), the binding energy of Zn^{2+} to MorphGE (−84.01 kJ·mol^{-1}) is much lower than that of Zn^{2+} to H_2O (−61.41 kJ·mol^{-1}), which confirms that Zn^{2+} prefers to coordinate with MorphGE to form the low-desolvation-energy structure of $[Zn(H_2O)_x]^{2+}$ ($x < 6$). The schematic solvation structures of Zn^{2+} in liquid electrolyte, PAAm gel electrolyte, and MorphGE are depicted in Fig. 2(k), which illustrates the advantage of MorphGE on stabilizing $[Zn(H_2O)_x]^{2+}(x < 6)$. As reported, the desolvation energies of Zn^{2+} in $[Zn(H_2O)_x]^{2+}$ ($x < 6$) are much lower than $[Zn(H_2O)_6]^{2+}$, which would significantly improve Zn/Zn^{2+} reversibility to provide excellent high rate performance [5, 11, 16].

3.3 Electrochemical performance of symmetrical Zn batteries

The interfacial electrochemical stability between MorphGE and Zn anode was evaluated by long-term cycling stability test in Zn/MorphGE/Zn symmetrical batteries. As illustrated in Fig. 3(a), with MorphGE, the Zn/MorphGE/Zn symmetrical cell provided an ultra-stable polarization voltage for more than 2,400 h at the current density of 1 mA·cm^{-2}, and areal capacity of 1 mA·h·cm^{-2}. On the contrary, the liquid electrolyte showed a quick short circuit after only 52 h at the current density of 1 mA·cm^{-2} (inset of Fig. 3(a)). Furthermore, with an unstable interfacial contact, the elastic PAAm gel electrolyte could only cycle for less than 120 h before wild fluctuation and short circuit at the low current density of 1 mA·cm^{-2} and areal capacity of 1 mA·h·cm^{-2}. In addition, the initial deposition and nucleation overpotential of MorphGE is also much lower than liquid electrolyte and PAAm gel electrolyte; the MorphGE-based battery is only around 50 mV, but liquid electrolyte-based and PAAm gel electrolyte-based batteries are both higher than 200 mV. Astonishingly, even at the ultra-high current density of 10 mA·cm^{-2} and areal capacity of 10 mA·h·cm^{-2}, the MorphGE-based cell can still exhibit stable cycling performance for more than 100 h (Fig. 3(b)). In contrast, the liquid electrolyte-based battery only cycled for around 10 h, and the elastic PAAm gel electrolyte could not cycle stably from the first plating step (Fig. S9 in the ESM). Significantly, at such high current density, the voltage hysteresis of MorphGE-based battery is still lower than 100 mV for more than 100 h. The electrochemical performance of MorphGE- and liquid electrolyte-based batteries at current density of 7.5 mA·cm^{-2} and areal capacity of 7.5 mA·h·cm^{-2} was also examined, where the MorphGE-based battery can keep stable for more than 200 h (Fig. S10 in the ESM).

Figure 3(c) shows the surface morphology of Zn metal anode with MorphGE after cycling for 40, 200, 400, and 2,000 h, respectively. Interestingly, a well-defined hexagonal structure of Zn metal instead of Zn dendrite started to form on Zn anode after 40 h, and kept well-shaped and randomly formed even after 2,000 h. As reported, this hexagonal Zn crystal could enable a homoepitaxially uniform deposition for Zn metal during stripping and plating, and effectively avoid dendrite formation [4]. Notably, benefitting from this unique nucleation and growth route, at the high current density of 7.5 mA·cm^{-2}, the Zn anode of MorphGE-based battery presents a dendrite-free surface from 1st to 10th cycle (Fig. S11 in the ESM), while dendrite and death Zn have already formed at the first cycle in the case of liquid electrolyte with glass fiber as the separator. The homoepitaxial deposition morphology

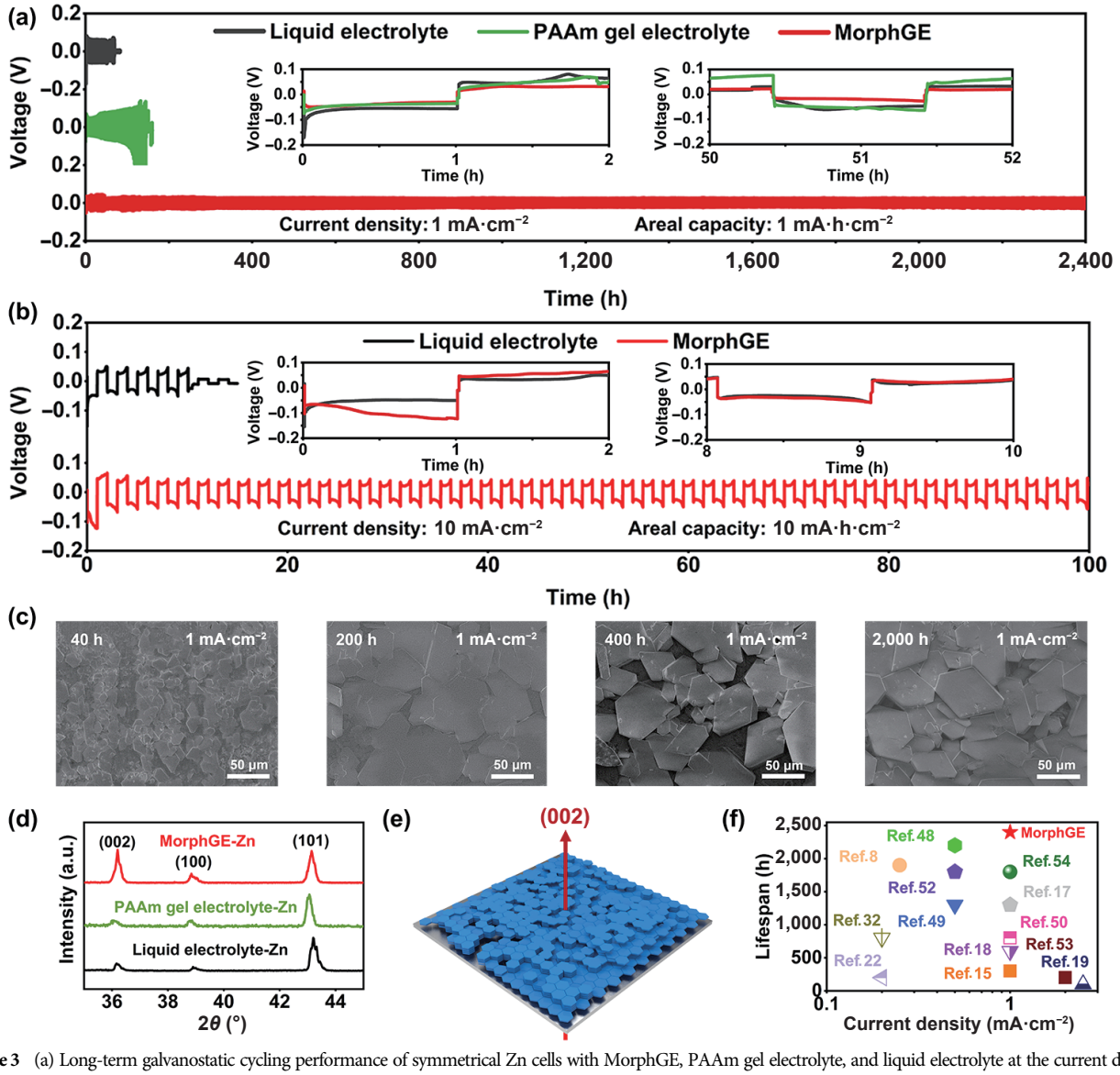

Figure 3 (a) Long-term galvanostatic cycling performance of symmetrical Zn cells with MorphGE, PAAm gel electrolyte, and liquid electrolyte at the current density of 1 mA·cm^{-2}, respectively. (b) Galvanostatic cycling performance of symmetrical Zn cells with MorphGE and liquid electrolyte at the current density of 10 mA·cm^{-2}, respectively. (c) SEM images of Zn metal anode at the current density of 1 mA·cm^{-2} for 40, 200, 400, and 2, 000 h. (d) XRD profiles of Zn anodes with MorphGE, PAAm gel electrolyte, and liquid electrolyte after cycling for 100 h at the current density of 1 mA·cm^{-2}. (e) Conceptual diagram of hexagonal Zn metal growth with MorphGE. (f) Comparison of the dendrite suppression performance of MorphGE-based Zn-ion battery with other reported ones.

to the horizontal direction (002) can be clearly seen in the detailed images (Fig. S12 in the ESM).

The XRD patterns of the Zn anode with liquid electrolyte, PAAm gel electrolyte, and MorphGE cycled after 100 h (1 mA·cm^{-2}) are provided in Fig. 3(d). The much higher (002) peak intensity of Zn in MorphGE-based batteries further confirms that Zn tends to grow laterally in the presence of MorphGE [4, 24]. On the contrary, the XRD patterns of the Zn metals cycled in liquid electrolyte and PAAm gel electrolyte for 100 h both provide a low (002) peak intensity, showing the random growth of Zn metal during stripping and plating. Low-angle (5°–30°) XRD profiles of MorphGE, PAAm gel electrolyte, and liquid electrolyte after cycling for 100 h at the current density of 1 mA·cm^{-2} were further examined for side reactions inspection (Fig. S13 in the ESM). According to the literature information [47], the by-products appear in four positions of 8.5°, 16.8°, 20.6°, and 24.8°. After 100 h, the liquid electrolyte curve shows the certain by-product peaks at 8.5°, 16.8°, and 24.8°, while the MorphGE and PAAm gel electrolyte groups show no obvious by-product peak in these areas. The cross-sectional SEM images of Zn anode in liquid electrolyte provided a clear and thick layer for around 34.6 μm, which is much thicker than that of the MorphGE (around 7.2 μm) (Fig. S14 in the ESM). This obvious difference convincingly demonstrates the inhibitory effect of MorphGE on dendrite growth [10]. The SEM images of the Zn metal with PAAm gel electrolyte after cycling (Fig. S15 in the ESM) further confirm this finding, where large amounts of vertically grown Zn dendrite can be observed. Figure 3(e) and Fig. S16 in the ESM show the hypothesized two situations of Zn metal nucleation in the cases of MorphGE and liquid electrolyte, respectively. Zn metal will nucleate and grow much uniformly in the presence of MorphGE, and form hexagonal Zn metal crystals to inhibit dendrite formation and improve the electrochemical stability and performance. Consequently, the battery performance is remarkably boosted even at the high current densities of 7.5 and 10 mA·cm^{-2}. Such a newly deposition feature in MorphGE supports the advantage of the good interfacial contact between Zn anode and MorphGE, which accounts for the superiority of MorphGE on Zn-ion batteries with the performance surpassing most literatures (see comparison in Fig. 3(f)) [8, 15, 17–19, 22, 32, 48–54].

3.4 Electrochemical performance of Zn/MnO_2 batteries

The ionic conductivities of MorphGE and liquid electrolyte were

measured by alternating current (AC) impedance spectra (Fig. 4(a) and Fig. S17 in the ESM). The ionic conductivity of MorphGE was calculated to be as high as 26.2 mS·cm^{-1}, almost two times higher than liquid electrolyte (9.35 mS·cm^{-1}). The high ionic conductivity can be ascribed to the salt enrichment effect in MorphGE as well as the faster desolvation ability brought by the regulated solvation structure [55]. Symmetrical Zn batteries were assembled and tested to calculate the Zn ion transference number of MorphGE (Fig. 4(b)). The transference number of Zn^{2+} calculated by the combination of chronoamperometry and impedance test is 0.65, also higher than liquid electrolyte (0.38) [9]. This may be attributed to the interactions between Zn^{2+} and cellulose hydroxyl groups, which remarkably reduce the transfer resistance arising from cellulose nanofibrils, and optimize Zn ion transfer path in the whole MorphGE.

We further synthesized MnO_2/CNT composite material and modulated it into a slurry to coat carbon paper as the cathode electrode, and CV test was performed at different scanning speeds, which verifies the excellent reversibility of the electrode material (Fig. S18 in the ESM). Then, Zn/MorphGE/MnO_2 battery was employed to evaluate the electrochemical performance of MorphGE. It is noteworthy that, as assembled with electrodes, the interlocked structure formed between MorphGE and cathode can be clearly observed due to the bulk plasticity of MorphGE (Fig. S19 in the ESM). As tested, the galvanostatic charge/discharge platforms of MorphGE-based Zn-ion batteries kept stable with the gradual increase in current density (Fig. S20 in the ESM). At the current densities of 308 (1 C), 616 (2 C), 1,540 (5 C), 3,080 (10 C), 6,160 mA·g^{-1} (20 C), the battery can deliver the reversible capacity as high as 241, 235, 205, 183, and 155 mA·h·g^{-1}, respectively (Fig. 4(c)). Surprisingly, even at the ultra-high current density of 7,700 mA·g^{-1} (25 C), the battery still delivered a high reversible specific capacity of 138 mA·h·g^{-1}, and kept a stable and reversible high specific capacity after returning back to 308 mA·g^{-1}. As for long-term cycling performance at the high current density of 6,160 mA·g^{-1} (20 C), the Zn-ion battery provided a prominent high capacity (100 mA·h·g^{-1}) and excellent stability (capacity retention as high as 98.5% for 500 cycles), as shown in Fig. 4(d). Long-term cycling stability of MorphGE-based battery at the current density of 3,080 mA·g^{-1} (10 C) was also tested (Fig. 4(e)), where the capacity retention can keep 99.2% after 2,000 cycles. Calendar life and cycling performance after rest are important factors in battery system, since the side reactions already occur during the rest period [21]. To demonstrate the advantage of our MorphGE, we aged the semi-cell for 120 h before cycling, and then cycled at the current density of 10 C. The battery aged for 120 h can still provide a reversible specific capacity as high as the battery without aging after 200 cycles, verifying the effect of the MorphGE on side reaction inhibition from the initial rest period (Fig. S21 in the ESM). The slightly higher capacity of the aged battery can be ascribing to the sufficient electrode infiltration during long time aging.

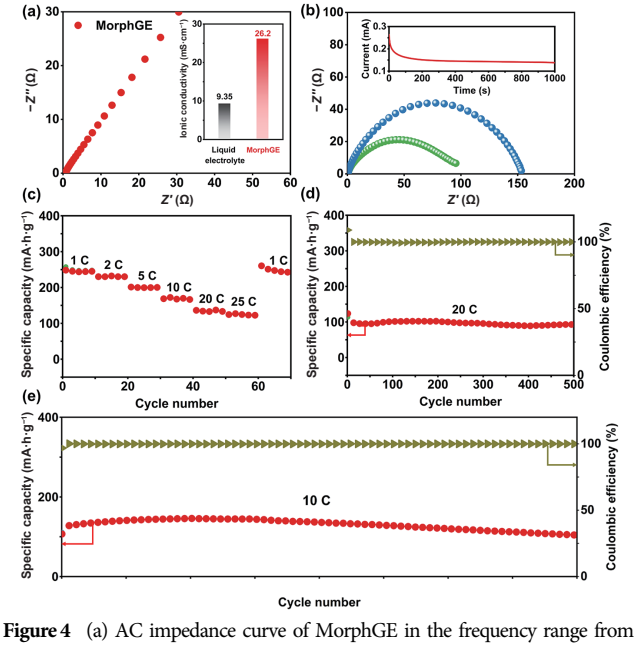

Figure 4 (a) AC impedance curve of MorphGE in the frequency range from 10 kHz to 0.1 Hz (inset: calculated ionic conductivities of MorphGE and liquid electrolyte). (b) Characterization of Zn^{2+} transference number in MorphGE by symmetrical Zn cell with an additional potential of 20 mV. (c) Rate performance of Zn-ion battery at various current densities from 1 to 25 C. (d) High-rate cycling performance and corresponding coulombic efficiency of MorphGE-based Zn-ion battery at 20 C. (e) Long-term cycling performance and corresponding coulombic efficiency of MorphGE-based Zn-ion battery at 10 C for 2, 000 cycles.

XRD and SEM images after 2,000 cycles were then provided. As shown, the (002) peak increased obviously, in accordance with the XRD results in Fig. 3(d). In addition, negligible by-product peaks can be observed for MorphGE-Zn after 2,000 cycles, demonstrating the effective side reaction inhibition performance for MorphGE (Fig. S22 in the ESM). SEM images (Fig. S23 in the ESM) before and after cycling also demonstrate the lateral growth of the Zn anode in MorphGE full batteries.

3.5 Flexible Zn-ion batteries

We finally demonstrate that the high-performance MorphGE-based Zn-ion battery may also be potentially used as flexible and wearable devices that require to be shaped or applied in some extreme environments. The quasi-solid-state Zn-ion battery was assembled in air, as illustrated in Fig. 5(a). The Zn metal anode and MnO_2 cathode were both loaded on carbon fiber cloth to achieve flexible electrodes. As shown in Fig. 5(b), attributing to the good interface contact between MorphGE and electrodes, at the current density of 1 C, the quasi-solid-state battery can deliver a high reversible capacity of 250 mA·h·g^{-1} for more than 100 cycles. Even when curved on an artificial finger, the battery can still provide a good capacity of around 220 mA·h·g^{-1} for 100 cycles (Fig. 5(c)). It is worth noting that the as-assembled quasi-solid battery performed extraordinarily well when subjected to the high-rate charge–discharge cycling test. As presented in Fig. 5(d), at the high current density of 5 C, the device exhibits a high and stable cycling performance for more than 500 cycles with a steady reversible capacity of 180 mA·h·g^{-1}. To further evaluate the safety and stability of MorphGE-based flexible Zn-ion batteries after being damaged in daily use, a number of destructive experiments were conducted, including multiple bending, hammering, puncturing, and cutting (Figs. 5(e)–5(h)). The quasi-solid batteries still worked normally, providing stable power supply for a digital thermo-hygrometer.

4 Conclusions

In this paper, we proposed a new strategy of mechanoadaptive cellulose nanofibril-based MorphGE to tackle the dendrite formation problem of Zn-ion batteries that is not easily solved by conventional rigid-elastic gel electrolytes. The MorphGE possesses both high modulus and bulk plasticity with a very short LVE region to guarantee both outstanding gel-electrode interfacial adaptability and dendrite suppressing ability. Moreover, the employed MorphGE has abundant cellulose hydroxyl groups to regulate Zn-ion solvation structures, resulting in both high ionic conductivity (26.2 mS·cm^{-1}) and Zn ion transference number (0.65). With these advantages, the as-fabricated Zn-ion battery can

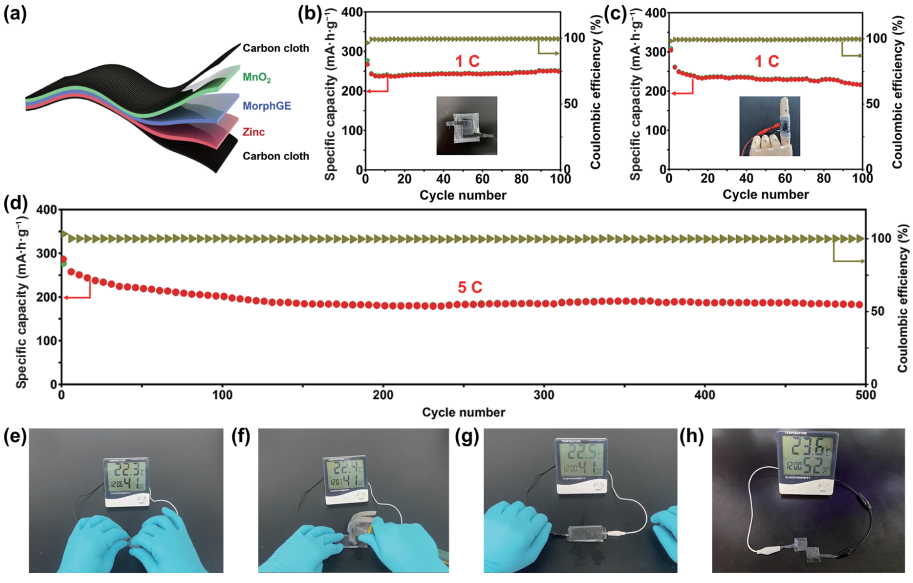

Figure 5 (a) Schematic diagram of MorphGE-based flexible Zn-ion battery. (b) Cycling performance of the flexible battery at 1 C. (c) Cycling performance at the bent state. (d) Long-term cycling performance of the flexible battery at 5 C. (e) Bending, (f) hammering, (g) puncturing, and (h) cutting tests for MorphGE-based flexible battery.

operate for more than 200 h at an ultra-high current density of 7.5 mA·cm^{-2}, and 100 h for 10 mA·cm^{-2}, on stripping and plating performance of symmetrical Zn cell. The battery can also deliver a reversible capacity of about 100 mA·h·g^{-1} at an ultra-high rate of 20 C and maintain the capacity retention of 98.5% after more than 500 cycles. Finally, MorphGE-based flexible battery device would still exhibit a reversible capacity of 180 mA·h·g^{-1} at the current density of 5 C for more than 500 cycles. Even as destroyed by hammering, bending, puncturing, and cutting, the flexible battery can steadily operate an electronic device. We believe such quasi-solid-electrolyte Zn-ion battery with low-cost, regenerate, and interfacially adaptive MorphGE will greatly promote the practical applications of Zn-ion batteries in next-generation wearable and flexible devices.

Acknowledgements

This work was supported by the National Science Foundation of China (NSFC) (Nos. 51903041, 21991123, and 51873035), Natural Science Foundation of Shanghai (No. 19ZR1470700), and "Qimingxing Plan" (No. 19QA1400200). The authors thank the staffs from BL16B beamline at Shanghai Synchrotron Radiation Facility for assistance during data collection.

Electronic Supplementary Material: Supplementary material (TEM, polarized optical images, tensile and rheological test of MorphGE; ATR-FTIR/XPS spectra of MorphGE, regenerated cellulose hydrogel, liquid electrolyte, and PAAm gel; cyclic performance of symmetrical Zn battery; SEM images of symmetrical Zn batteries after cycling; ionic conductivity of liquid electrolyte; TEM and SEM images, XRD curves and CV test of MnO_2/CNT cathodes; optical images of MorphGE and MnO_2/CNT cathode surface after battery assembly; rate performance of MorphGE; comparison of dendrite suppression performance of Zn-ion batteries) is available in the online version of this article at https://doi.org/10.1007/s12274-021-3770-8.

References

[1] Pomerantseva, E.; Bonaccorso, F.; Feng, X. L.; Cui, Y.; Gogotsi, Y. Energy storage: The future enabled by nanomaterials. *Science* **2019**, *366*, eaan8285.

[2] Li, Y. B.; Fu, J.; Zhong, C.; Wu, T. P.; Chen, Z. W.; Hu, W. B.; Amine, K.; Lu, J. Batteries: Recent advances in flexible zinc-based rechargeable batteries (Adv. Energy Mater. 1/2019). *Adv. Energy Mater.* **2019**, *9*, 1970001.

[3] Ming, J.; Guo, J.; Xia, C.; Wang, W. X.; Alshareef, H. N. Zinc-ion batteries: Materials, mechanisms, and applications. *Mater. Sci. Eng.: R: Rep.* **2019**, *135*, 58–84.

[4] Zheng, J. X.; Zhao, Q.; Tang, T.; Yin, J. F.; Quilty, C. D.; Renderos, G. D.; Liu, X. T.; Deng, Y.; Wang, L.; Bock, D. C. et al. Reversible epitaxial electrodeposition of metals in battery anodes. *Science* **2019**, *366*, 645–648.

[5] Zhu, M. S.; Wang, X. J.; Tang, H. M.; Wang, J. W.; Hao, Q.; Liu, L. X.; Li, Y.; Zhang, K.; Schmidt, O. G. Antifreezing hydrogel with high zinc reversibility for flexible and durable aqueous batteries by cooperative hydrated cations. *Adv. Funct. Mater.* **2020**, *30*, 1907218.

[6] Mo, F. N.; Liang, G. J.; Meng, Q. Q.; Liu, Z. X.; Li, H. F.; Fan, J.; Zhi, C. Y. A flexible rechargeable aqueous zinc manganese-dioxide battery working at −20 °C. *Energy Environ. Sci.* **2019**, *12*, 706–715.

[7] Wang, Z. Q.; Hu, J. T.; Han, L.; Wang, Z. J.; Wang, H. B.; Zhao, Q. H.; Liu, J. J.; Pan, F. A MOF-based single-ion Zn^{2+} solid electrolyte leading to dendrite-free rechargeable Zn batteries. *Nano Energy* **2019**, *56*, 92–99.

[8] Leng, K. T.; Li, G. J.; Guo, J. J.; Zhang, X. Y.; Wang, A. X.; Liu, X. J.; Luo, J. Y. A safe polyzwitterionic hydrogel electrolyte for long-life quasi-solid state zinc metal batteries. *Adv. Funct. Mater.* **2020**, *30*, 2001317.

[9] Zhao, Z. M.; Zhao, J. W.; Hu, Z. L.; Li, J. D.; Li, J. J.; Zhang, Y. J.; Wang, C.; Cui, G. L. Long-life and deeply rechargeable aqueous Zn anodes enabled by a multifunctional brightener-inspired interphase. *Energy Environ. Sci.* **2019**, *12*, 1938–1949.

[10] Ma, L. T.; Chen, S. M.; Li, N.; Liu, Z. X.; Tang, Z. J.; Zapien, J. A.; Chen, S. M.; Fan, J.; Zhi, C. Y. Hydrogen-free and dendrite-dree all-solid-state Zn-ion batteries. *Adv. Mater.* **2020**, *32*, 1908121.

[11] Yang, H. J.; Chang, Z.; Qiao, Y.; Deng, H.; Mu, X. W.; He, P.; Zhou, H. S. Constructing a super-saturated electrolyte front surface for stable rechargeable aqueous zinc batteries. *Angew. Chem., Int. Ed.* **2020**, *59*, 9377–9381.

[12] Chao, D. L.; Zhu, C.; Song, M.; Liang, P.; Zhang, X.; Tiep, N. H.; Zhao, H. F.; Wang, J.; Wang, R. M.; Zhang, H. et al. A high-rate and stable quasi-solid-state zinc-ion battery with novel 2D layered zinc orthovanadate array. *Adv. Mater.* **2018**, *30*, 1803181.

[13] Liu, C. F.; Neale, Z.; Zheng, J. Q.; Jia, X. X.; Huang, J. J.; Yan, M. Y.; Tian, M.; Wang, M. S.; Yang, J. H.; Cao, G. Z. Expanded hydrated vanadate for high-performance aqueous zinc-ion batteries. *Energy Environ. Sci.* **2019**, *12*, 2273–2285.

[14] Liu, H.; Cheng, X. B.; Huang J. Q.; Yuan, H.; Lu, Y.; Yan, C.; Zhu, G. L.; Xu, R.; Zhao, C. Z.; Hou, L. P. et al. Controlling dendrite

growth in solid-state electrolytes. *ACS Energy Lett.* **2020**, *5*, 833–843.

[15] Xia, A. L.; Pu, X. M.; Tao, Y. Y.; Liu, H. M.; Wang, Y. G. Graphene oxide spontaneous reduction and self-assembly on the zinc metal surface enabling a dendrite-free anode for long-life zinc rechargeable aqueous batteries. *Appl. Surf. Sci.* **2019**, *481*, 852–859.

[16] Cui, Y. H.; Zhao, Q. H.; Wu, X. J.; Chen, X.; Yang, J. L.; Wang, Y. T.; Qin, R. Z.; Ding, S. X.; Song, Y. L.; Wu, J. W. et al. An interface-bridged organic–inorganic layer that suppresses dendrite formation and side reactions for ultra-long-life aqueous zinc metal anodes. *Angew. Chem., Int. Ed.* **2020**, *59*, 16594–16601.

[17] Liu, X. Q.; Yang, F.; Xu, W.; Zeng, Y. X.; He, J. J.; Lu, X. H. Zeolitic imidazolate frameworks as Zn^{2+} modulation layers to enable dendrite-free Zn anodes. *Adv. Sci.* **2020**, *7*, 2002173.

[18] Li, C.; Sun, Z. T.; Yang, T.; Yu, L. H.; Wei, N.; Tian, Z. N.; Cai, J. S.; Lv, J. Z.; Shao, Y. L.; Rümmeli, M. H. et al. Directly grown vertical graphene carpets as Janus separators toward stabilized Zn metal anodes. *Adv. Mater.* **2020**, *32*, 2003425.

[19] Kim, J. Y.; Liu, G. C.; Shim, G. Y.; Kim, H.; Lee, J. K. Functionalized Zn@ZnO hexagonal pyramid array for dendrite-free and ultrastable zinc metal anodes. *Adv. Funct. Mater.* **2020**, *30*, 2004210.

[20] Zhang, N. N.; Huang, S.; Yuan, Z. S.; Zhu, J. C.; Zhao, Z. F.; Niu, Z. Q. Direct self-assembly of MXene on Zn anodes for dendrite-free aqueous zinc-ion batteries. *Angew. Chem., Int. Ed.* **2021**, *60*, 2861–2865.

[21] Li, Q.; Wang, Y. B.; Mo, F. N.; Wang, D. H.; Liang, G. J.; Zhao, Y. W.; Yang, Q.; Huang, Z. D.; Zhi, C. Y. Calendar life of Zn batteries based on Zn anode with Zn powder/current collector structure. *Adv. Energy Mater.* **2021**, *11*, 2003931.

[22] Xu, W. N.; Zhao, K. N.; Huo, W. C.; Wang, Y. Z.; Yao, G.; Gu, X.; Cheng, H. W.; Mai, L.; Hu, C. G.; Wang, X. D. Diethyl ether as self-healing electrolyte additive enabled long-life rechargeable aqueous zinc ion batteries. *Nano Energy* **2019**, *62*, 275–281.

[23] Zhao, J. W.; Zhang, J.; Yang, W. H.; Chen, B. B.; Zhao, Z. M.; Qiu, H. Y.; Dong, S. M.; Zhou, X. H.; Cui, G. L.; Chen, L. Q. "Water-in-deep eutectic solvent" electrolytes enable zinc metal anodes for rechargeable aqueous batteries. *Nano Energy* **2019**, *57*, 625–634.

[24] Chang, N. N.; Li, T. Y.; Li, R.; Wang, S. N.; Yin, Y. B.; Zhang, H. M.; Li, X. F. An aqueous hybrid electrolyte for low-temperature zinc-based energy storage devices. *Energy Environ. Sci.* **2020**, *13*, 3527–3535.

[25] Cao, L. S.; Li, D.; Hu, E. Y.; Xu, J. J.; Deng, T.; Ma, L.; Wang, Y.; Yang, X. Q.; Wang, C. S. Solvation structure design for aqueous Zn metal batteries. *J. Am. Chem. Soc.* **2020**, *142*, 21404–21409.

[26] Yuan, D.; Zhao, J.; Ren, H.; Chen, Y. Q.; Chua, R.; Jie, E. T. J.; Cai, Y.; Edison, E.; Manalastas, W. Jr.; Wong, M. W. et al. Anion texturing towards dendrite-free Zn anode for aqueous rechargeable batteries. *Angew. Chem., Int. Ed.* **2021**, *60*, 7213–7219.

[27] Mo, F. N.; Chen, Z.; Liang, G. J.; Wang, D. H.; Zhao, Y. W.; Li, H. F.; Dong, B. B.; Zhi, C. Y. Zwitterionic sulfobetaine hydrogel electrolyte building separated positive/negative ion migration channels for aqueous Zn-MnO_2 batteries with superior rate capabilities. *Adv. Energy Mater.* **2020**, *10*, 2000035.

[28] Qiu, H. Y.; Du, X. F.; Zhao, J. W.; Wang, Y. T.; Ju, J. W.; Chen, Z.; Hu, Z. L.; Yan, D. P.; Zhou, X. H.; Cui, G. L. Zinc anode-compatible in-situ solid electrolyte interphase via cation solvation modulation. *Nat. Commun.* **2019**, *10*, 5374.

[29] Li, H. F.; Han, C. P.; Huang, Y.; Huang, Y.; Zhu, M. S.; Pei, Z. X.; Xue, Q.; Wang, Z. F.; Liu, Z. X.; Tang, Z. J. et al. An extremely safe and wearable solid-state zinc ion battery based on a hierarchical structured polymer electrolyte. *Energy Environ. Sci.* **2018**, *11*, 941–951.

[30] Zhang, Q. C.; Li, C. W.; Li, Q. L.; Pan, Z. H.; Sun, J.; Zhou, Z. Y.; He, B.; Man, P.; Xie, L. Y.; Kang, L. X. et al. Flexible and high-voltage coaxial-fiber aqueous rechargeable zinc-ion battery. *Nano Lett.* **2019**, *19*, 4035–4042.

[31] Li, H. F.; Liu, Z. X.; Liang, G. J.; Huang, Y.; Huang, Y.; Zhu, M. S.; Pei, Z. X.; Xue, Q.; Tang, Z. J.; Wang, Y. K. et al. Waterproof and tailorable elastic rechargeable yarn zinc ion batteries by a cross-linked polyacrylamide electrolyte. *ACS Nano* **2018**, *12*, 3140–3148.

[32] Han, Q.; Chi, X. W.; Zhang, S. M.; Liu, Y. Z.; Zhou, B.; Yang, J. H.; Liu, Y. Durable, flexible self-standing hydrogel electrolytes enabling high-safety rechargeable solid-state zinc metal batteries. *J. Mater. Chem. A* **2018**, *6*, 23046–23054.

[33] Huang, S.; Wan, F.; Bi, S. S.; Zhu, J. C.; Niu, Z. Q.; Chen, J. A self-healing integrated all-in-one zinc-ion battery. *Angew. Chem., Int. Ed.* **2019**, *58*, 4313–4317.

[34] Wu, H. P.; Cao, Y.; Su, H. P.; Wang, C. Tough gel electrolyte using double polymer network design for the safe, stable cycling of lithium metal anode. *Angew. Chem., Int. Ed.* **2018**, *57*, 1361–1365.

[35] Ye, F.; Zhang, X.; Liao, K. M.; Lu, Q.; Zou, X. H.; Ran, R.; Zhou, W.; Zhong, Y. J.; Shao, Z. P. A smart lithiophilic polymer filler in gel polymer electrolyte enables stable and dendrite-free Li metal anode. *J. Mater. Chem. A* **2020**, *8*, 9733–9742.

[36] Wang, D. H.; Li, H. F.; Liu, Z. X.; Tang, Z. J.; Liang, G. J.; Mo, F. N.; Yang, Q.; Ma, L. T.; Zhi, C. Y. A nanofibrillated cellulose/polyacrylamide electrolyte-based flexible and sewable high-performance Zn-MnO_2 battery with superior shear resistance. *Small* **2018**, *14*, 1803978.

[37] Liu, K.; Pei, A.; Lee, H. R.; Kong, B.; Liu, N.; Lin, D. C.; Liu, Y. Y.; Liu, C.; Hsu, P. C.; Bao, Z. N. et al. Lithium metal anodes with an adaptive "solid-liquid" interfacial protective layer. *J. Am. Chem. Soc.* **2017**, *139*, 4815–4820.

[38] Luo, Y. F.; Li, W. L.; Lin, Q. Y.; Zhang, F. L.; He, K.; Yang, D. P.; Loh, X. J.; Chen, X. D. A morphable ionic electrode based on thermogel for non-invasive hairy plant electrophysiology. *Adv. Mater.* **2021**, *33*, 2007848.

[39] Liu, Y. X.; Li, J. X.; Song, S.; Kang, J.; Tsao, Y.; Chen, S. C.; Mottini, V.; McConnell, K.; Xu, W. H.; Zheng, Y. Q. et al. Morphing electronics enable neuromodulation in growing tissue. *Nat. Biotechnol.* **2020**, *38*, 1031–1036.

[40] Zhang, X. T.; Wu, B. H.; Sun, S. T.; Wu, P. Y. Hybrid materials from ultrahigh-inorganic-content mineral plastic hydrogels: Arbitrarily shapeable, strong, and tough. *Adv. Funct. Mater.* **2020**, *30*, 1910425.

[41] Cao, Z. Y.; Zhuang, P. Y.; Zhang, X.; Ye, M. X.; Shen, J. F.; Ajayan, P. M. Strategies for dendrite-free anode in aqueous rechargeable zinc ion batteries. *Adv. Energy Mater.* **2020**, *10*, 2001599.

[42] Mredha, M. T. I.; Le, H. H.; Tran, V. T.; Trtik, P.; Cui, J. X.; Jeon, I. Anisotropic tough multilayer hydrogels with programmable orientation. *Mater. Horiz.* **2019**, *6*, 1504–1511.

[43] Pedersen, J. S.; Schurtenberger, P. Scattering functions of semiflexible polymers with and without excluded volume effects. *Macromolecules* **1996**, *29*, 7602–7612.

[44] Xu, Q.; Chen, C.; Rosswurm, K.; Yao, T. M.; Janaswamy, S. A facile route to prepare cellulose-based films. *Carbohydr. Polym.* **2016**, *149*, 274–281.

[45] Zhang, X. F.; Hou, T.; Chen, J.; Feng, Y.; Li, B. G.; Gu, X. L.; He, M.; Yao, J. F. Facilitated transport of CO_2 through the transparent and flexible cellulose membrane promoted by fixed-site carrier. *ACS Appl. Mater. Interfaces* **2018**, *10*, 24930–24936.

[46] Zhang, X. F.; Ma, X. F.; Hou, T.; Guo, K. C.; Yin, J. Y.; Wang, Z. G.; Shu, L.; He, M.; Yao, J. F. Inorganic salts induce thermally reversible and anti-freezing cellulose hydrogels. *Angew. Chem., Int. Ed.* **2019**, *58*, 7366–7370.

[47] Cong, J. L.; Shen, X.; Wen, Z. P.; Wang, X.; Peng, L. Q.; Zeng, J.; Zhao, J. B. Ultra-stable and highly reversible aqueous zinc metal anodes with high preferred orientation deposition achieved by a polyanionic hydrogel electrolyte. *Energy Stor. Mater.* **2021**, *35*, 586–594.

[48] Hao, J. N.; Li, X. L.; Zhang, S. L.; Yang, F. H.; Zeng, X. H.; Zhang, S.; Bo, G. Y.; Wang, C. S.; Guo, Z. P. Designing dendrite-free zinc anodes for advanced aqueous zinc batteries. *Adv. Funct. Mater.* **2020**, *30*, 2001263.

[49] Qin, R. Z.; Wang, Y. T.; Zhang, M. Z.; Wang, Y.; Ding, S. X.; Song, A. Y.; Yi, H. C.; Yang, L. Y.; Song, Y. L.; Cui, Y. H. et al. Tuning Zn^{2+} coordination environment to suppress dendrite formation for high-performance Zn-ion batteries. *Nano Energy* **2021**, *80*, 105478.

[50] Zeng, X. H.; Liu, J. T.; Mao, J. F.; Hao, J. N.; Wang, Z. J.; Zhou, S.; Ling, C. D.; Guo, Z. P. Toward a reversible Mn^{4+}/Mn^{2+} redox

reaction and dendrite-free Zn anode in near-neutral aqueous Zn/MnO_2 batteries via salt anion chemistry. *Adv. Energy Mater.* **2020**, *10*, 1904163.

[51] Cui, M. W.; Xiao, Y.; Kang, L. T.; Du, W.; Gao, Y. F.; Sun, X. Q.; Zhou, Y. L.; Li, X. M.; Li, H. F.; Jiang, F. Y. et al. Quasi-isolated Au particles as heterogeneous seeds to guide uniform Zn deposition for aqueous zinc-ion batteries. *ACS Appl. Energy Mater.* **2019**, *2*, 6490–6496.

[52] Dong, L. B.; Yang, W.; Yang, W.; Tian, H.; Huang, Y. F.; Wang, X. L.; Xu, C. J.; Wang, C. Y.; Kang, F. Y.; Wang, G. X. Flexible and conductive scaffold-stabilized zinc metal anodes for ultralong-life zinc-ion batteries and zinc-ion hybrid capacitors. *Chem. Eng. J.* **2020**, *384*, 123355.

[53] Zeng, Y. X.; Zhang, X. Y.; Qin, R. F.; Liu, X. Q.; Fang, P. P.; Zheng, D. Z.; Tong, Y. X.; Lu, X. H. Dendrite-free zinc deposition induced by multifunctional CNT frameworks for stable flexible Zn-ion batteries. *Adv. Mater.* **2019**, *31*, 1903675.

[54] Ma, L. T.; Chen, S. M.; Li, X. L.; Chen, A.; Dong, B. B.; Zhi, C. Y. Liquid-free All-Solid-State zinc batteries and encapsulation-free flexible batteries enabled by *in situ* constructed polymer electrolyte. *Angew. Chem., Int. Ed.* **2020**, *59*, 23836–23844.

[55] Song, Z. S.; Ding, J.; Liu, B.; Liu, X. R.; Han, X. P.; Deng, Y. D.; Hu, W. B.; Zhong, C. A rechargeable Zn-air battery with high energy efficiency and long life enabled by a highly water-retentive gel electrolyte with reaction modifier. *Adv. Mater.* **2020**, *32*, 1908127.